Effect of Nb^{3+} Substitution on the Structural, Magnetic, and Optical Properties of Co$_{0.5}$Ni$_{0.5}$Fe$_2$O$_4$ Nanoparticles

Munirah. A. Almessiere [1,2] , **Yassine Slimani** [1] , **Murat Sertkol** [3] , **Muhammed Nawaz** [4] ,
Ali Sadaqat [5] , **Abdulhadi Baykal** [4,*] , **Ismail Ercan** [1] **and Bekir Ozçelik** [6]

[1] Department of Biophysics, Institute for Research and Medical Consultations (IRMC), Imam Abdulrahman Bin Faisal University, P.O. Box 1982, Dammam 31441, Saudi Arabia; malmessiere@iau.edu.sa (M.A.A.); yaslimani@iau.edu.sa (Y.S.); iercan@iau.edu.sa (I.E.)

[2] Department of Physics, College of Science, Imam Abdulrahman Bin Faisal University, P.O. Box 1982, Dammam 31441, Saudi Arabia

[3] Deanship of Preparatory Year, Imam Abdulrahman Bin Faisal University, P.O. Box 1982, Dammam 31441, Saudi Arabia; msertkol@iau.edu.sa

[4] Department of Nanomedicine Research, Institute for Research and Medical Consultations (IRMC), Imam Abdulrahman Bin Faisal University, P.O. Box 1982, Dammam 31441, Saudi Arabia; mnnmuhammad@iau.edu.sa

[5] Mechanical and Energy Engineering Department, College of Engineering, Imam Abdulrahman Bin Faisal University, P.O. Box 1982, Dammam 31441, Saudi Arabia; sadali@iau.edu.sa

[6] Department of Physics, Faculty of Science and Letters, Cukurova University, Balcali-Adana 01330, Turkey; ozcelik@cu.edu.tr

* Correspondence: abaykal@iau.edu.sa

Abstract: Co$_{0.5}$Ni$_{0.5}$Nb$_x$Fe$_{2-x}$O$_4$ (0.00 $\leq$ x $\leq$ 0.10) nanoparticles (NPs) were prepared using the hydrothermal approach. The X-ray powder diffraction (XRD) pattern confirmed the formation of single-phase spinel ferrite. The crystallite size was found to range from 18 to 26 nm. The lattice parameters were found to increase with greater Niobium ion (Nb^{3+}) concentration, caused by the variance in the ionic radii between the Nb^{3+} and Fe^{3+}. Fourier transform infrared analysis also proved the existence of the spinal ferrite phase. The percent diffuse reflectance (%DR) analysis showed that the value of the band gap increased with growing Nb^{3+} content. Scanning electron microscopy and transmission electron microscopy revealed the cubic morphology. The magnetization analyses at both room (300 K, RT) and low (10 K) temperatures exhibited their ferromagnetic nature. The results showed that the Nb^{3+} substitution affected the magnetization data. We found that Saturation magnetization (M_s), Remanence (M_r), and the Magnetic moment (n_B) decreased with increasing Nb^{3+}. The squareness ratio (SQR) values at RT were found to be smaller than 0.5, which postulate a single domain nature with uniaxial anisotropy for all produced ferrites. However, different samples exhibited SQRs within 0.70 to 0.85 at 10 K, which suggests a magnetic multi-domain with cubic anisotropy at a low temperature. The obtained magnetic results were investigated in detail in relation to the structural and microstructural properties.

Keywords: spinel ferrites; Nb substitution; low temperature magnetization; optical properties; TEM analysis

1. Introduction

Spinel ferrite nanoparticle materials are highly preferred in engineering and technology applications like biomedicine, pharmaceuticals, sensors, magnetic resonance imaging, drug delivery,

microwaves, high-frequency devices, information storage, and electronic chips [1–4]. The structure and electromagnetic properties of nano-spinel ferrites can be modified by the substitution of different cations. Rare earth substitutions are highly valuable for reducing the particle size and intensification of the lattice parameter [5]. In this respect, substituting rare earth (RE) cations into the spinel ferrite structure plays an important role in enhancing the dielectric, magnetic, and electric properties due to the Fe–Fe interactions caused by the spin coupling effect of 3d electrons [6]. Therefore, electrical and magnetic behavior may change when rare earth and iron interactions (3d–4f coupling) of the spinel ferrites occur. Different RE substitutions have been proven to have different results on the ferrite structure [7–9]. Many researchers have investigated the effects of RE substitution into cobalt spinel ferrite ($CoFe_2O_4$) in bulk form, thin film, and nanoparticles [10–12]. Coercivity, anisotropic constant, and uniaxial anisotropy were described as decreasing with the addition of m and Ce ions into nano-cobalt ferrites [13]. Several methods have been used to synthesize nickel-substituted cobalt ferrites, $Co_{1-x}Ni_xFe_2O_4$, such as the auto-combustion method, aerosol route, and co-precipitation method [14–16]. Chen et al. [17] prepared $Ni_{1-x}Co_xFe_2O_4$ nanoparticles (NPs) using the hydrothermal method and studied the increasing trend in saturation magnetization with increasing cobalt content, which occurred due to the substitution of an Ni^{2+} ion to a Co^{2+} ion. Maz et al. [18] synthesized $Co_{1-x}Ni_xFe_2O_4$ nanoparticles in a chemical co-precipitation process and noticed the increasing trend of coercivity (H_c) and saturation magnetization (M_s) with increasing cobalt content.

Coercivity (H_c) and saturation magnetization (M_s) values were shown to decrease with an increase in the Ni content in $Co_{1-x}Mn_xFe_2O_4$ ($0.0 \leq x \leq 0.4$) nanoparticles [19]. A few papers have been published on Nd^{3+} ion-substituted cobalt-ferrite in the Fe sites. Almessiere et al. [20] reported the effect of the magnetocrystalline anisotropy constant decreasing with the addition of Nd^{3+} ions in cobalt spinel nano-ferrites $Co_{1-2x}Ni_xMn_xFe_{2-y}Nd_yO_4$ ($0.0 \leq x = y \leq 0.3$) synthesized using the sol-gel method. Yadav et al. [21] examined the magnetic and structural properties by incorporating Nd^{3+} ions in cobalt spinel ferrite nanoparticles, $CoFe_{2-x}Nd_xO_4$ ($x \leq 0.1$), synthesized using the sol-gel method. Tahar et al. [22] investigated the RE = La, Ho, Tb, Ce, Gd, Nd, and Sm substitutions in $CoFe_{1.9}RE_{0.1}O_4$ nanoparticles. Aside from these RE substitutions, Nd^{3+} ions considerably decrease the coercivity and saturation magnetization. Zhao et al. [23] reported that coercivity and saturation magnetization slightly increased with Nd^{3+} substitution in cobalt ferrite nanocrystals $CoFe_{2-x}Nd_xO_4$ synthesized by the emulsion method. In this study, the effect of Nb^{3+} substituted in the Co-Ni spinel ferrite on the structural, optical, and magnetic properties are discussed in detail.

2. Experimental Materials and Methods

2.1. Materials and Instruments

A Rigaku Benchtop Miniflex X-ray diffraction (XRD) diffractometer (Tokyo, Japan) with Cu K_α radiation at room temperature (RT) over the 2θ range from 20° to 70° was used for the structural analysis. Scanning electron microscopy (SEM, FEI Titan ST, Hillsboro, OR, USA) along with energy dispersive X-ray spectroscopy (EDX) and transmission electron microscopy (TEM; FEI, Morgagni 268, Prague, Czech Republic) were used for the morphological and composition analyses. Spectral analysis of all products was performed via Fourier transform infrared (FT-IR) spectroscopy (Bruker, Berlin, Germany). Ultraviolet-visible (UV-vis) diffuse reflectance (DR%, Shimadzu, Tokyo, Japan) spectra were recorded in the 200 to 800 nm wavelength range using a DR spectrophotometer. The magnetic properties of the products were measured using a Quantum Design SQUID-PPMS vibrating sample magnetometer (PPMS DynaCool, Quantum Design, San Diego, CA, USA).

Cobalt (II) nitrate ($Co(NO_3)_2$), nickel (II) nitrate ($Ni(NO_3)_2$), iron (III) nitrate hexahydrate ($Fe(NO_3)_3.6H_2O$), and niobium (V) nitrate ($Nb(NO_3)_5$) were received from Sigma-Aldrich (St. Louis, MO, USA) and used as received.

2.2. Procedure

The hydrothermal method approach was used to synthesize $Co_{0.5}Ni_{0.5}Nb_xFe_{2-x}O_4$ ($0.00 \leq x \leq 0.10$) nanoparticles. Stoichiometric amounts of iron, nickel, and cobalt nitrates were dissolved in 50 mL deionized (DI) H_2O. Niobium nitrate was dissolved in concentrated HCl in a separate beaker with vigorous stirring. Then, the two solutions were mixed together and stirred for an extra 30 min and the pH of the resulting solution was adjusted to 11 by adding sodium hydroxide (NaOH) with continuous stirring for 30 min. Before transfer to a Teflon-lined vessel, the mixture was pretreated in an ultrasonic water bath for 30 to 40 min. The final solution was transferred to a stainless-steel Teflon autoclave (200 mL) and placed in an oven at 180 °C for 10 h. The resulting product was washed with hot deionized water three times and left to dry overnight at 80 °C for 5 h.

3. Results and Discussion

3.1. XRD Analysis

Figure 1 displays the crystal structure of the $Co_{0.5}Ni_{0.5}Nb_xFe_{2-x}O_4$ ($0.00 \leq x \leq 0.10$) nanoparticles. The XRD analysis showed the signature peaks of a single phase of Co spinel ferrite with no presence of any extra secondary phase, which means that the Nb^{3+} was well dissolved in the Co–Ni crystal. Only the x = 0.02 sample had a minor amount of the Fe_2O_3 phase as an impurity. The structural parameters were calculated through Rietveld refinement using the XRD experimental data, as registered in Table 1. We found that the lattice parameters increased with the rise in the Nb^{3+} amount due to the larger ionic radius of Nb^{3+} (0.72 Å) in comparison with Fe^{3+} (0.64 Å), which caused stress in the lattice. The crystallite sizes were estimated to range from 18 to 26 nm.
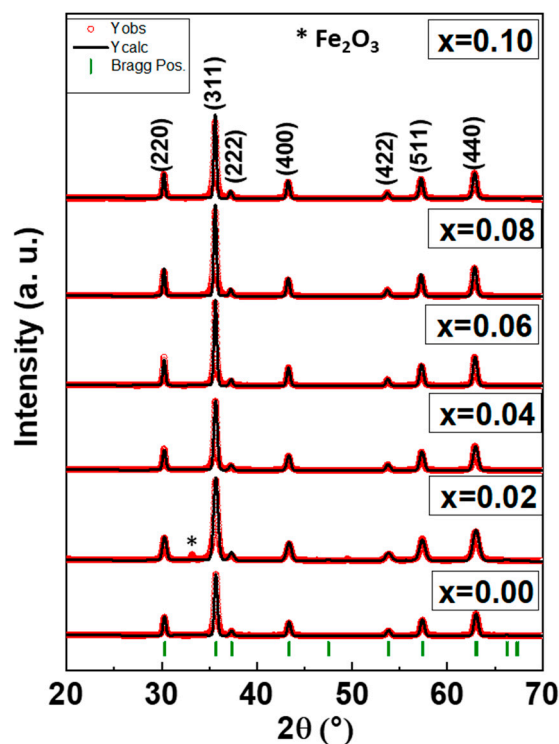

Figure 1. X-ray diffraction (XRD) powder patterns of the $Co_{0.5}Ni_{0.5}Nb_xFe_{2-x}O_4$ ($0.0 \leq x \leq 1.0$) nanoparticles.

Table 1. Nb content and refined structural parameters (a is the lattice parameter, V is the volume of the cell, D_{XRD} is the crystallite size obtained from the broadening of the highest peak by using the Scherrer method, χ^2(chi^2) is the squared ratio, R_{Bragg} is the Bragg factor) for the $Co_{0.5}Ni_{0.5}Nb_xFe_{2-x}O_4$ ($0 \leq x \leq 1.0$) nanoparticles.

x	a (Å)	V (Å)^3	D_{XRD} (nm) $\pm$ 0.09	χ^2(chi^2)	R_{Bragg}
0.00	8.345 (1)	581.15	22.86	1.75	12.67
0.02	8.345 (9)	581.33	18.71	1.32	3.12
0.04	8.352 (3)	582.67	24.18	1.52	3.99
0.06	8.356 (6)	583.57	27.59	1.32	2.48
0.08	8.362 (3)	584.76	26.86	1.77	7.88
0.10	8.362 (4)	584.77	24.70	1.32	8.77

3.2. Spectral Analysis

Figure 2 highlights the FT-IR spectra of $Co_{0.5}Ni_{0.5}Nb_xFe_{2-x}O_4$ ($0.00 \leq x \leq 0.10$). The strongest stretching bands at 584.36 and 410.7 cm^{-1} represent the Co spinel ferrite structure. These bands can be attributed to the stretching of the vibration band between F and O. The vibration bands shifted toward higher wavenumbers when the Nb^{3+} content increased, which was due to the variation in the bond length as a result of the larger ionic radii of Nb^{3+} [24–26].
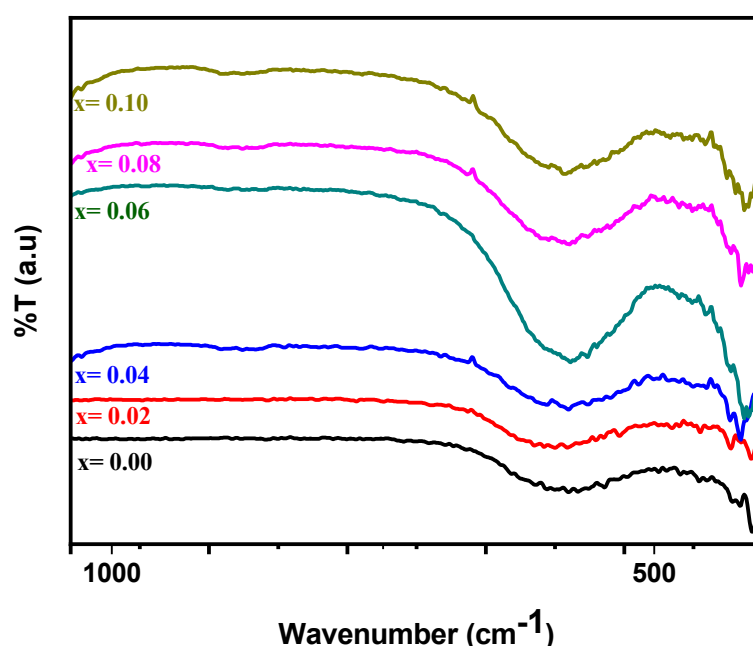

Figure 2. Fourier transform infrared (FT-IR) spectra of the $Co_{0.5}Ni_{0.5}Nb_xFe_{2-x}O_4$ ($0.0 \leq x \leq 1.0$) nanoparticles.

3.3. Morphological Analysis

The Field emission scanning electron microscope (FE-SEM) microstructure of the $Co_{0.5}Ni_{0.5}Nb_xFe_{2-x}O_4$ ($0.00 \leq x \leq 0.10$) nanoparticles is depicted in Figure 3. The images exhibited a higher agglomeration cubic shape with an average grain size of less than 27 nm, which agreed with the crystal size estimated by XRD. The EDX spectrum and elemental mapping confirmed the existence of Co, Ni, Nb, and O in compositions x = 0.02 and 0.06, as shown in Figure 4. The quantitative analysis of selected samples that recorded the atomic weigh of x = 0.02 and 0.06 showed that the estimated values were close to the expected values for the samples. The TEM and SAED (Selected area electron diffraction) pattern of the $Co_{0.5}Ni_{0.5}Nb_xFe_{2-x}O_4$ (x = 0.06) nanoparticles are shown in Figure 5. The images confirmed the cubic spinel structure and aggregate.
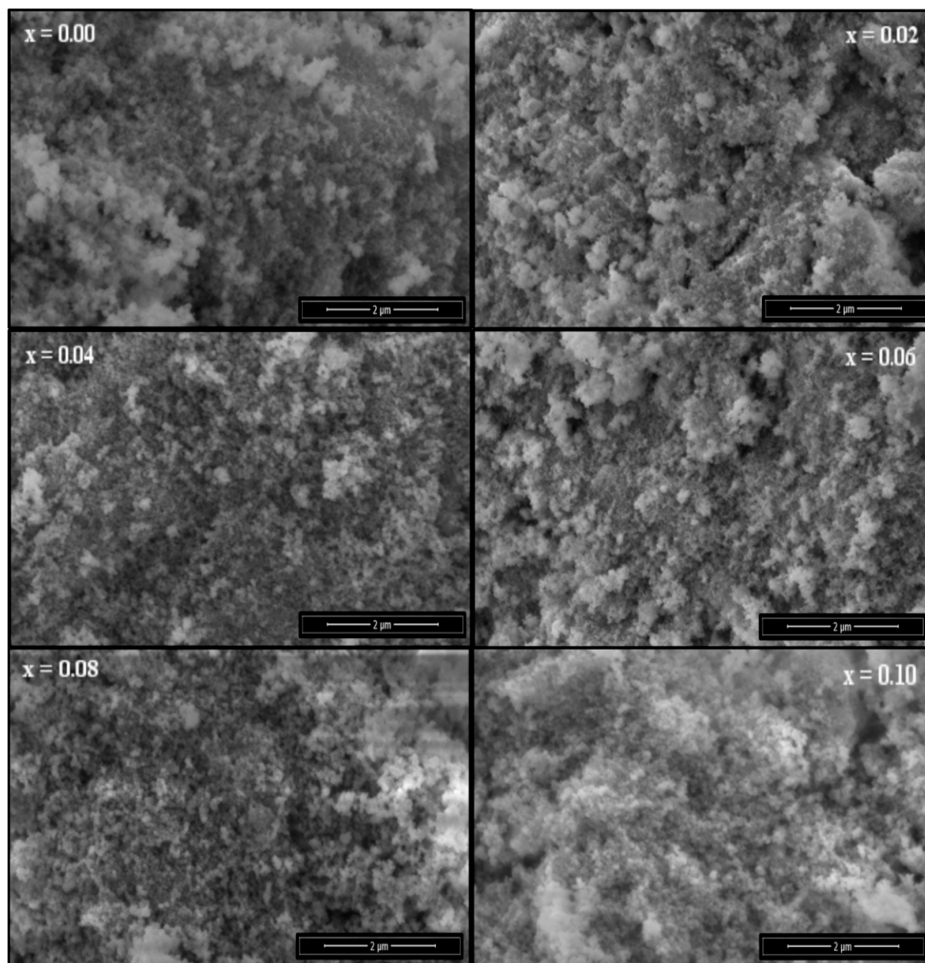
Figure 3. Scanning electron microscope (SEM) micrographs of the $Co_{0.5}Ni_{0.5}Nb_xFe_{2-x}O_4$ ($0.0 \leq x \leq 0.10$) nanoparticles.

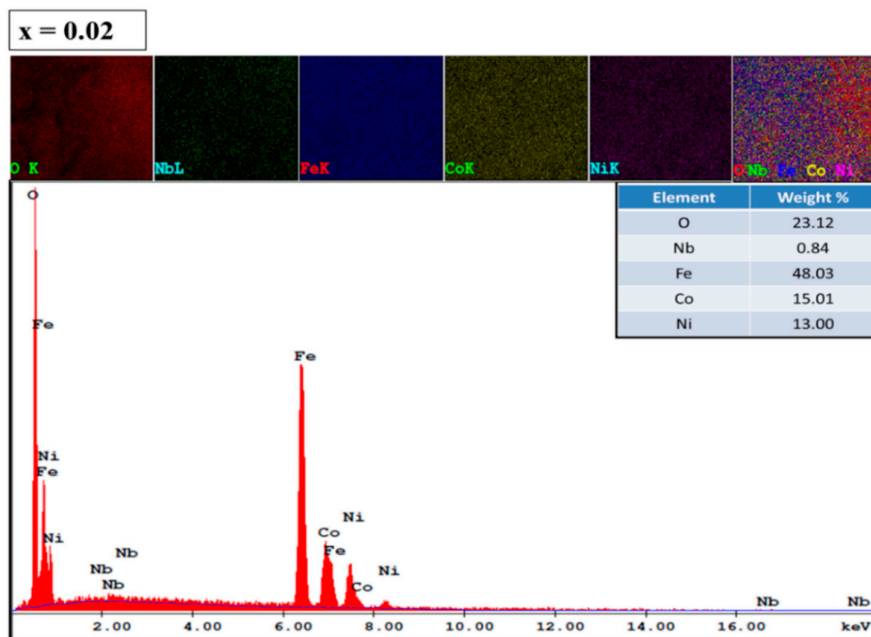| Element	Weight %
O	23.12
Nb	0.84
Fe	48.03
Co	15.01
Ni	13.00

Figure 4. *Cont.*

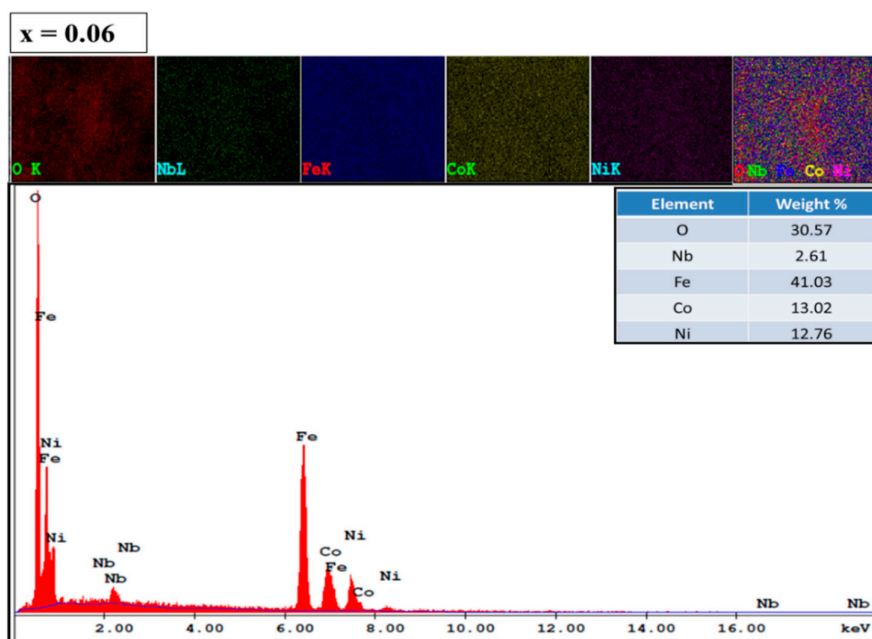**Figure 4.** Energy dispersive X-ray (EDX) spectrographs and elemental mapping images of the $Co_{0.5}Ni_{0.5}Nb_xFe_{2-x}O_4$ nanoparticles for x = 0.02 and 0.06.

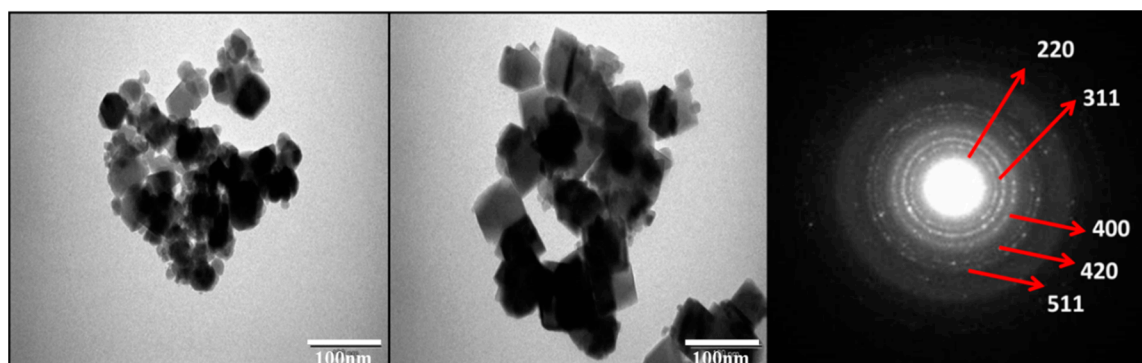**Figure 5.** Transmission electron diffraction (TEM) images (with different magnetization) and selected area electron diffraction (SAED) pattern of $Co_{0.5}Ni_{0.5}Nb_xFe_{2-x}O_4$ for x = 0.06 nanoparticles.

3.4. Optical Analysis

The optical properties of $Co_{0.5}Ni_{0.5}Nb_xFe_{2-x}O_4$ ($0.00 \leq x \leq 0.10$) nanoparticles were studied using a DR-UV-visible spectrophotometer ranging from 200 to 800 nm. Figure 6 shows that the compositions at different concentrations exhibited spectra in the visible range. The Kubelka–Munk model was used to compute the optical band gap energy (E_g) [27]. The band gap energy was calculated using a plot of $(\alpha hv)^2$ vs. photon energy (hv), which is also called the Tauc plot, of the $Co_{0.5}Ni_{0.5}Nb_xFe_{2-x}O_4$ ($0.00 \leq x \leq 0.10$) nanoparticles (Figure 7).

The band gap values were 0.25, 0.35, 0.51, 0.72, 0.76, and 0.77 eV for x = 0.00, 0.02, 0.04, 0.06, 0.08, and 0.1, respectively. When the value of x increased, the band gap value increased. The increase in the band gap value was ascribed to the development of the energy level or interface defects in M. Almessiere et al. [28]. The increase in the band gap could also be due to the synergistic effect of nano-ferrite with niobium, which decreases the electron hole recombination [29].
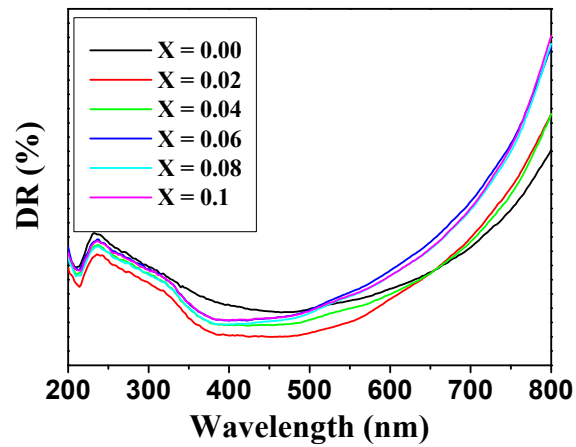
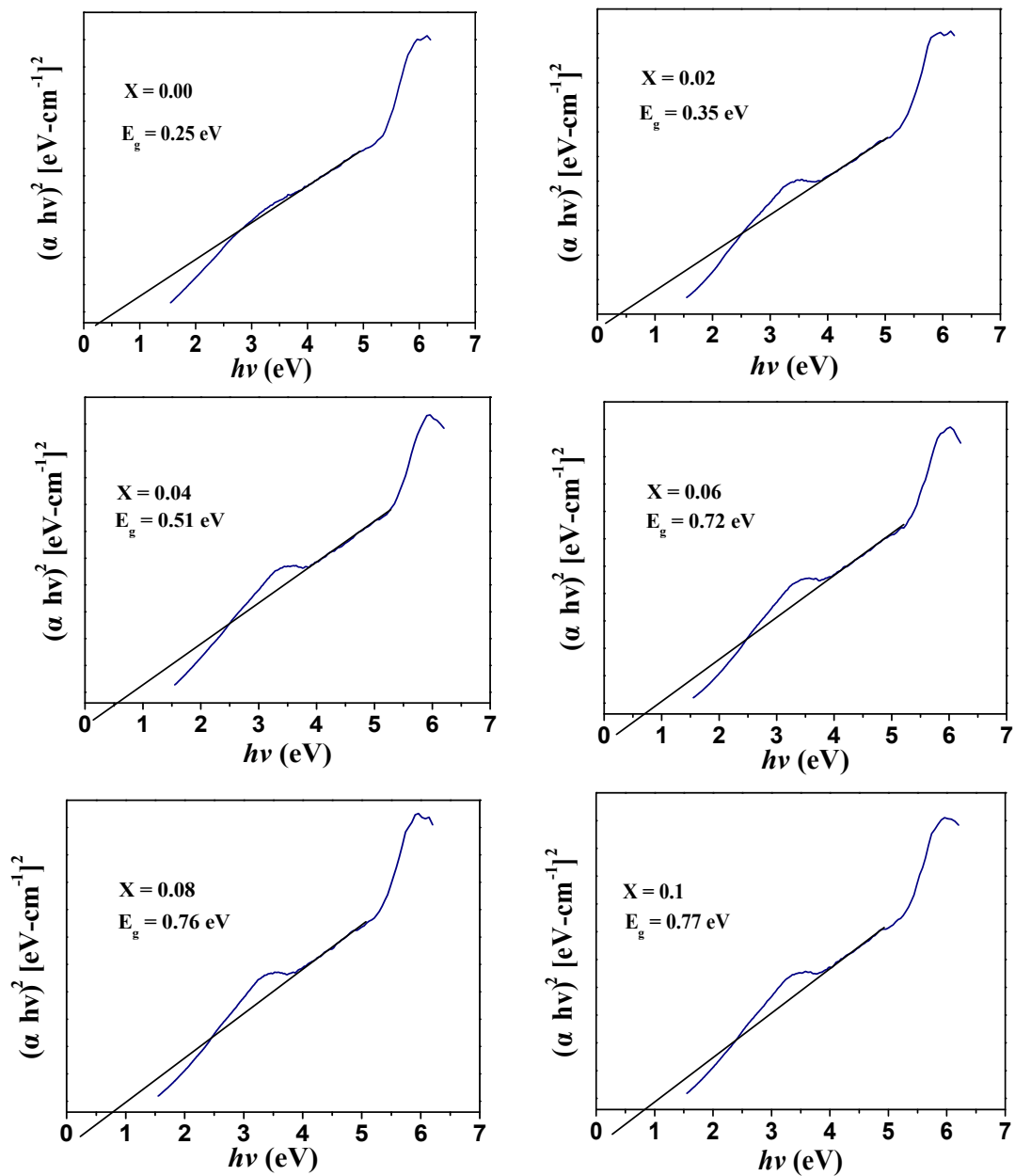**Figure 6.** DR% spectra of the $Co_{0.5}Ni_{0.5}Nb_xFe_{2-x}O_4$ ($0.0 \leq x \leq 0.10$) nanoparticles.

Figure 7. $[\alpha hv]^2$ versus hv graphs of the $Co_{0.5}Ni_{0.5}Nb_xFe_{2-x}O_4$ ($0.0 \leq x \leq 0.10$) nanoparticles.

3.5. Magnetization Investigations

The magnetization plots against an applied magnetic field of ± 20 kOe, M(H) for all the $Co_{0.5}Ni_{0.5}Nb_xFe_{2-x}O_4$ ($0.00 \leq x \leq 0.10$) nanoparticles performed at RT are illustrated in Figure 8. Table 2 summarizes the various deduced magnetic parameters for all the $Co_{0.5}Ni_{0.5}Nb_xFe_{2-x}O_4$ ($0.00 \leq x \leq 0.10$) nanoparticles at RT. The Nb^{3+} substitution in the Fe^{3+} sites altered the magnetic properties of the CoNi ferrite. The different CoNi ferrites displayed remanence magnetization (M_r) ranging from 13.00 to 23.66 emu/g. H_c ranged from 207.31 to 1129.92 Oe. The $M_{max,20}$ (magnetization at a maximum field of 20 kOe) was found to be between 42.36 and 49.77 emu/g. The Stoner–Wohlfarth (S–W) theory was used to extract the saturation magnetization (M_s) [30–32]. An example of the estimation of M_s for the x = 0.00 sample is shown in Figure 9. The extrapolation of this plot at high magnetic fields approaching zero produces the M_s value. The M_s values of the $Co_{0.5}Ni_{0.5}Nb_xFe_{2-x}O_4$ ($0.00 \leq x \leq 0.10$) nanoparticles ranged from 43.15 to 50.62 emu/g at RT. According to the obtained findings, we confirmed that the differently produced $Co_{0.5}Ni_{0.5}Nb_xFe_{2-x}O_4$ ($0.00 \leq x \leq 0.10$) nanoparticles have a soft ferromagnetic (FM) nature at RT.

Table 2. Magnetic parameters of the $Co_{0.5}Ni_{0.5}Nb_xFe_{2-x}O_4$ ($0 \leq x \leq 1.0$) nanoparticles at room temperature (RT) ($M_{max,20}$: max magnetization at 20 kOe, M_s: saturation magnetization, M_r: remanence magnetization, K_a: magnetic anisotropy constant, SQR: squareness ratio, H_c: coercivity and n_B: magnetic moment).

x	$M_{max,20}$ (emu/g)	M_s (emu/g)	M_r (emu/g)	K_a (Erg/g)	SQR	H_c (Oe)	n_B (μ_B)
0.00	49.77	50.62	18.47	1.96×10^5	0.365	648.11	2.13
0.02	47.98	48.81	20.9	1.74×10^5	0.428	509.9	2.06
0.04	46.57	47.36	13	1.78×10^5	0.274	286.11	2.00
0.06	45.68	46.52	23.66	2.16×10^5	0.509	1129.92	1.97
0.08	43.93	44.71	18.5	1.77×10^5	0.414	775.67	1.90
0.10	42.36	43.15	13.48	1.63×10^5	0.312	207.31	1.84

The M(H) were also performed for all of the $Co_{0.5}Ni_{0.5}Nb_xFe_{2-x}O_4$ ($0.00 \leq x \leq 0.10$) nanoparticles at 10 K (Figure 10). The deduced magnetic parameters at 10 K are listed in Table 3. H_c ranged from 708.93 to 5882.24 Oe. M_r ranged from 34.11 to 48.09 emu/g. The $M_{max,20}$ values ranged from 45.36 to 57.22 emu/g. M_s varied from 45.71 to 57.96 emu/g. Spinel ferrite nanoparticles have been reported to have a superparamagnetic threshold below 10 nm [33]. Since our nanoparticles had dimensions larger than 10 nm, the effect of the superparamagnetic state nanoparticles on lower magnetization was neglected. The obtained magnetic results at 10 K revealed the semi-hard FM nature of all products. Compared to 300 K, the M_s, M_r, and H_c showed a remarkable increase at 10 K. This increase was due to reduced thermal fluctuations of the magnetic moments [34,35]. In the literature, the anisotropy contribution of RE ions has been reported via spin-orbit coupling when they occupy the B sites of spinel ferrites [31,36]. This is one of the reasons for the observation of higher coercivities at CoMn ferrites doped with rare-earth ions.

At both measurement temperatures, the x = 0.00 sample had the highest magnitudes of M_s, which were about 49.77 and 57.22 emu/g at 300 and 10 K, respectively. Likewise, the x = 0.00 product exhibited the maximum M_r values with magnitudes of 18.47 and 48.09 emu/g at 300 and 10 K, respectively. The magnetization magnitudes found in the present study for the non-substituted sample were comparable to those of the $CoFe_2O_4$ and $NiFe_2O_4$ inverse spinel ferrites [37,38], but they are larger than those reported in the literature for $Co_{0.5}Ni_{0.5}Fe_2O_4$ [39]. The obtained magnitudes were smaller than those reported for both the bulk $CoFe_2O_4$ and $NiFe_2O_4$ inverse spinel ferrites [33,40]. The lower M_s and M_r magnitudes, in comparison to that of the bulk samples, were largely attributed to the smaller crystallite size, which leads to a structural disorder on the surface since the spin

disorder will be significant when the volume and surface ratio are important [41]. Spin canting as a result of antiferromagnetic interaction competition, the construction of a magnetic inactive layer, the non-collinear arrangement of the magnetic moments of Fe^{3+} ions, and the disordered cations distributions on the surface could all explain the lowered magnetization magnitudes [42,43].
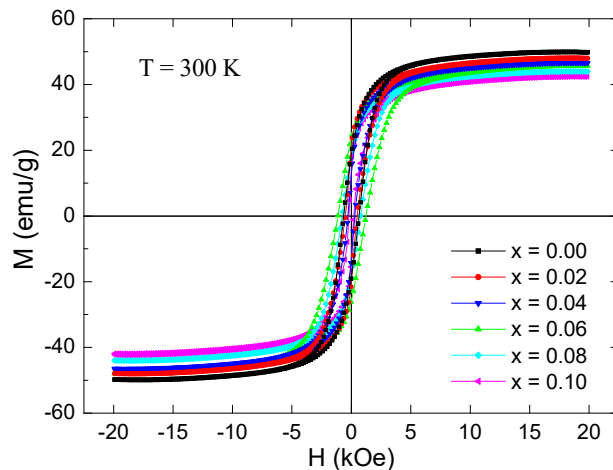

Figure 8. Magnetization versus applied field of ±20 kOe, M(H), for the $Co_{0.5}Ni_{0.5}Fe_{2-x}O_4$ ($0.0 \leq x \leq 0.10$) nanoparticles at RT.

Table 3. The deduced magnetic parameters of the $Co_{0.5}Ni_{0.5}Nb_xFe_{2-x}O_4$ ($0 \leq x \leq 1.0$) nanoparticles at 10 K ($M_{max,20}$: max magnetization at 20 kOe, Ms: saturation magnetization, Mr: remanence magnetization, Ka: magnetic anisotropy constant, SQR: squareness ratio, H_c: coercivity, and n_B: magnetic moment).

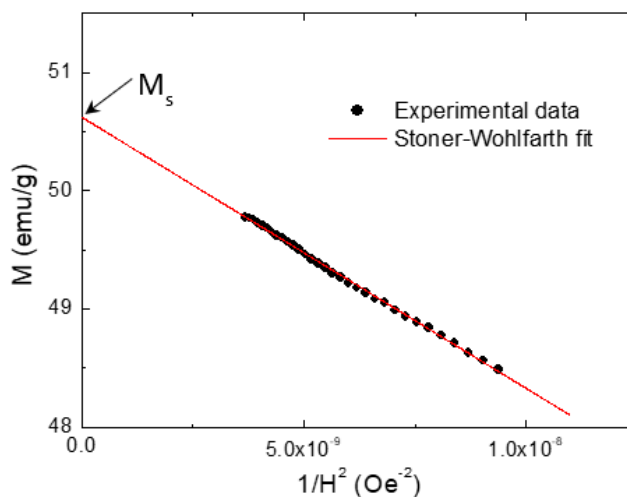| x	$M_{max,20}$ (emu/g)	M_s (emu/g)	M_r (emu/g)	K_a (Erg/g)	SQR	H_c (Oe)	n_B (μ_B)
0.00	57.22	57.96	48.09	4.30×10^5	0.830	5335.84	2.43
0.02	54.44	55.25	44.47	3.98×10^5	0.805	4760.39	2.33
0.04	53.53	54.26	44.24	3.78×10^5	0.815	3440.9	2.29
0.06	51.23	52.05	44.08	5.24×10^5	0.847	5882.24	2.21
0.08	48.39	48.62	34.11	3.57×10^5	0.702	2848	2.07
0.10	45.36	45.71	34.94	2.67×10^5	0.764	708.93	1.95

Figure 9. A schematic example of the M vs. $1/H^2$ plot for the $Co_{0.5}Ni_{0.5}Fe_2O_4$ nanoparticles at RT.

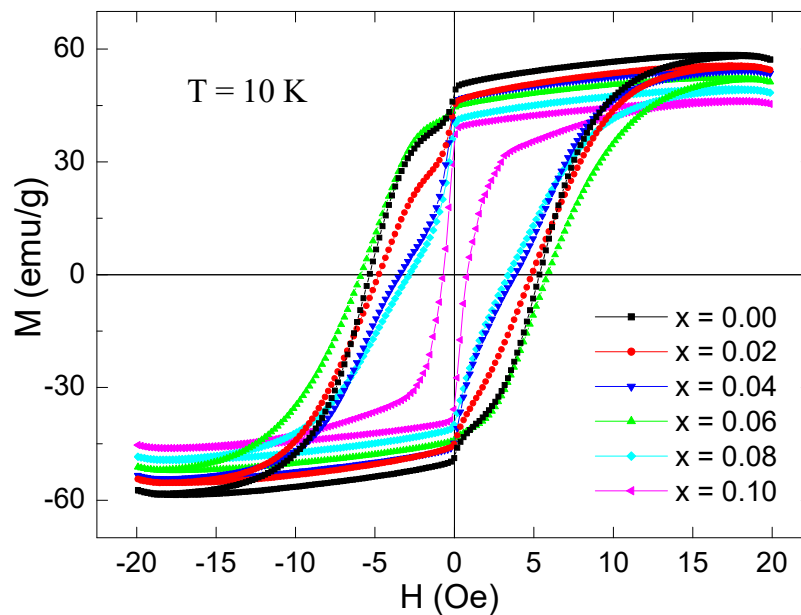**Figure 10.** Magnetization against an applied field of ±20 kOe, M (H), for all of the $Co_{0.5}Ni_{0.5}Fe_{2-x}O_4$ ($0.0 \leq x \leq 0.10$) nanoparticles at 10 K.

At both temperatures, the highest H_c was observed for x = 0.06 and the lowest for x = 0.10. Various parameters governed the coercivity, like grain size, magnetic particle morphology, magnetocrystalline anisotropy, strains and exchange coupling between the collinear spins in the core, and the canted spins on the surface [34,35]. The improvement in coercive field can be principally attributed to the increase of magnetocrystalline anisotropy [44,45]. Equation (1) describes the proportionality between the coercivity H_c and magnetic anisotropy constant K_a [44].

$$H_c \propto \frac{2K_a}{\mu_o M_s} \tag{1}$$

where μ_o is the permeability constant. When the magnetic anisotropy increases with increasing substitution content, coercivity grows. To determine the anisotropy constant K_a, the expression used to estimate the values of M_s according to the S–W fit is shown below [31,32].

$$M = M_s \left(1 - \frac{\beta}{H^2}\right) \tag{2}$$

Consequently, the slope of the linear fitting provides the constant β, which is related to the magnetocrystalline anisotropy constant K_a. Once the values of the β constant are determined, the magnetic anisotropy constant (K_a) can be estimated by using the equation below [31,32].

$$K_a = M_s \left(\frac{15\,\beta}{4}\right)^{\frac{1}{2}} \tag{3}$$

The deduced K_a values at 300 and 10 K are listed in Tables 2 and 3, respectively. The magnetocrystalline anisotropy was the maximum for the x = 0.06 product and was the minimum for x = 0.10. This result explains the highest coercivity in the x = 0.06 sample.

The Nb^{3+} substitution led to a gradual reduction in the M_s and M_r values. The lowest magnitudes were observed for the $Co_{0.5}Ni_{0.5}Fe_{1.9}Nb_{0.1}O_4$ (x = 0.1) sample. The minimum M_s values belonging to the x = 0.1 product were about 43.15 and 45.71 emu/g at 300 and 10 K, respectively. The minimum M_r for x = 0.1 were 13.00 and 34.11 emu/g at 300 and 10 K, respectively. The evolutions in the M_r values showed a similar trend to M_s with respect to the Nb^{3+} concentration. It has been reported previously

that evolutions in the M_r values depend principally on evolutions in M_s and on the net alignment of magnetization grains derived from super-exchange interactions between the magnetic particles [32].

Numerous factors can affect the magnetic properties of spinel ferrites, including the crystallite size change, variations in magnetic moments (n_B), variations in the nature and concentration of different sites, and the preferred site occupancy of different ions [36]. The local strains and the super-exchange interactions between different ions might influence the magnetic parameters [34,35]. Principally, the magnetic moment of spinel ferrites is derived from the iron ions and their distribution in the crystal sites. The A–A and B–B interactions were unimportant. However, the A–B exchange interactions were dominant. Consequently, any factors that affect the strength of various exchange interactions will modify the magnetization. In our case, the observed decrease in M_s and M_r values with Nb^{3+} substitution was attributable to the weakening of the exchange interactions in the Fe sites. The ions of the host Fe^{3+} (0.62 Å) displayed a slightly smaller ionic radius when compared to that of Nb^{3+} (0.72 Å). The contrast of magnetic moments and ionic radii of the host and substituted ions might produce a non-collinear ferromagnetic arrangement and local strains that cause the disorder and variations in electronic states in the hexaferrite systems [32,34,35]. The substitution of Fe^{3+} ions with Nb^{3+} ions resulted in increasing the distance separating the magnetic ions and, therefore, decreasing the strength of the A–B super-exchange interactions. The relation between the magnetic moment (n_B) and M_s is given by the formula below [36].

$$n_B = \frac{Molecular\ Weight \times M_s}{5585}$$

The estimated n_B values of all of the $Co_{0.5}Ni_{0.5}Nb_xFe_{2-x}O_4$ ($0.00 \leq x \leq 0.10$) nanoparticles at 300 and 10 K are summarized in Tables 2 and 3, respectively. The decrease in n_B values resulting from the weakening of the super-exchange interactions among the various sites led to a decrease in the n_B values. In our case, n_B was found to decrease with increasing Nb^{3+} content. The x = 0.00 sample where the M_s value was the highest displayed the greatest n_B. The x = 0.10 sample where the M_s value was the lowest displayed the lowest n_B. This indicates a weakening of the super-exchange interactions.

The squareness ratios ($SQR = M_r/M_s$) were calculated for all the $Co_{0.5}Ni_{0.5}Nb_xFe_{2-x}O_4$ ($0.00 \leq x \leq 0.10$) nanoparticles at 300 and 10 K. According to the S–W theory, the SQR can take two values including one around 0.83 associated with the cubic anisotropy, and another around 0.5 that corresponds to uniaxial anisotropy [30,32]. The findings of SQR equal to or above 0.5 indicated that the particles were in the single magnetic domain, and those below 0.5 could be attributed to the formation of a multi-domain structure [46]. As can be seen from the tables, the SQR at RT was found to be around 0.509 for the x = 0.06 sample, which suggests a single magnetic domain with uniaxial anisotropy. However, the other samples displayed $SQRs$ that ranged from 0.31 to 0.42, which were less than 0.50 and can be attributed to surface spin disorder effects. This SQR was lower than 0.5, which indicates the formation of a multi-domain structure with uniaxial anisotropy. At 10 K, the different samples were found to have $SQRs$ ranging between 0.70 and 0.85, which are greater than 0.5. This suggests a single magnetic domain with cubic anisotropy.

4. Conclusions

A series of Nd^{3+}-substituted Co-Ni ferrite was synthesized via the hydrothermal approach. The XRD and FT-IR analyses proved the existence of single-phase spinel Co-ferrite. TEM analyses showed the hexagonal morphology of the products with minor agglomeration. The optical results showed that the band gap of the $Co_{0.5}Ni_{0.5}Nb_xFe_{2-x}O_4$ ($0.00 \leq x \leq 0.10$) nanoparticles were 0.25, 0.35, 0.51, 0.72, 0.76, and 0.77 eV, respectively. The M(H) analyses showed an FM comportment at both RT and 10 K for the $Co_{0.5}Ni_{0.5}Nb_xFe_{2-x}O_4$ ($0.00 \leq x \leq 0.10$) nanoparticles. The magnetic parameters strongly depend on temperature and Nb substitution content. The deduced M_s, M_r, and n_B values were the highest for the x = 0.00 sample and decreased with increasing Nb substitution. This effect is due to the weakening of super-exchange interactions, the creation of local strains, the preferred site

occupancy, and the decrease in the magnetic moments (n_B) with respect to the Nb content. The SQR values at RT were found to be smaller than 0.5, which postulates a single domain nature with uniaxial anisotropy for all the produced ferrites. However, the different samples exhibited SQRs in the 0.70–0.85 range at 10 K, which suggests a magnetic multi-domain with cubic anisotropy at a low temperature.

Author Contributions: Synthesis of the sample (A.B., M.A.A., and Y.S.). Investigation of the magnetic properties and writing (Y.S.). XRD analysis (M.S.). Participated in drafting the article or revising it critically for important intellectual content (S.A.). Optical analysis (M.N.). Gave final approval of the version to be submitted and any revised version (M.A.A., A.B., and Y.S.). Supervision, review, and editing (Y.S., A.B., and M.A.A.).

Conflicts of Interest: The authors declare no conflict of interest.

References

1. Chen, Q.; Zhang, Z.J. Size-dependent super paramagnetic properties of spinel ferrite nanocrystallites. *Appl. Phys. Lett.* **1998**, *73*, 3156. [CrossRef]
2. Zhao, L.; Yang, H.; Yu, L.; Cui, Y.; Zhao, X.; Feng, S. Magnetic properties of resubstituted Ni–Mn ferrite nanocrystallites. *J. Mater. Sci.* **2007**, *42*, 686–691. [CrossRef]
3. Kumar, E.R.; Kamzin, A.S.; Janani, K. Effect of annealing on particle size, microstructure and gas sensing properties of Mn substituted $CoFe_2O_4$ nanoparticles. *J. Magn. Magn. Mater.* **2016**, *417*, 122–129. [CrossRef]
4. Kumar, E.R.; Jayaprakash, R.; Patel, R. Structural and morphological studies of manganese substituted $CoFe_2O_4$ and $NiFe_2O_4$ nanoparticles. *Superlattices Microstruct.* **2013**, *62*, 277–284. [CrossRef]
5. Dascalu, G.; Popescu, T.; Feder, M.; Caltun, O.F. Structural, electric and magnetic properties of $CoFe_{1.8}RE_{0.2}O_4$ (RE = Dy, Gd, La) bulk materials. *J. Magn. Magn. Mater.* **2013**, *333*, 69–74. [CrossRef]
6. Shah, M.S.; Ali, K.; Ali, I.; Mahmood, A.; Ramay, S.M.; Farid, M.T. Structural and magnetic properties of praseodymium substituted barium-based spinel ferrites. *Mater. Res. Bull.* **2018**, *98*, 77–82. [CrossRef]
7. Junaid, M.; Khan, M.A.; Iqbal, F.; Murtaza, G.; Akhtar, M.N.; Ahmad, M.; Shakir, I.; Warsi, M.F. Structural, spectral, dielectric and magnetic properties of Tb–Dy doped Li-Ni nano-ferrites synthesized via micro-emulsion route. *J. Magn. Magn. Mater.* **2016**, *419*, 338–344. [CrossRef]
8. Boda, N.; Boda, G.; Naidu, K.C.B.; Srinivas, M.; Batoo, K.M.; Ravinder, D.; Reddy, A.P. Effect of rare earth elements on low temperature magnetic properties of Ni and Co-ferrite nanoparticles. *J. Magn. Magn. Mater.* **2019**, *473*, 228–235. [CrossRef]
9. Kokare, M.K.; Jadhav, N.A.; Singh, V.; Rathod, S.M. Effect of Sm^{3+} substitution on the structural and magnetic properties of Ni-Co nanoferrites. *Opt. Laser Technol.* **2019**, *112*, 107–116. [CrossRef]
10. Karimi, Z.; Mohammadifar, Y.; Shokrollahi, H.; Asl, S.K.; Yousefi, G.; Karimi, L. Magnetic and structural properties of nano sized Dy-doped cobalt ferrite synthesized by co-precipitation. *J. Magn. Magn. Mater.* **2014**, *361*, 150–156. [CrossRef]
11. Ghone, D.M.; Mathe, V.L.; Patankar, K.K.; Kaushik, S.D. Microstructure, lattice strain, magnetic and magnetostriction properties of holmium substituted cobalt ferrites obtained by co-precipitation method. *J. Alloys Compd.* **2018**, *739*, 52–61. [CrossRef]
12. Wu, X.; Ding, Z.; Song, N.; Li, L.; Wang, W. Effect of the rare-earth substitution on the structural, magnetic and adsorption properties in cobalt ferrite nanoparticles. *Ceram. Int.* **2016**, *42*, 4246–4255. [CrossRef]
13. Ahmad, S.I.; Ansari, S.A.; Kumar, D.R. Structural, morphological, magnetic properties and cation distribution of Ce and Sm co-substituted nano crystalline cobalt ferrite. *Mater. Chem. Phys.* **2018**, *208*, 248–257. [CrossRef]
14. Amir, M.; Baykal, A.; Sertkol, M.; Sözeri, H. Microwave Assisted Synthesis and Characterization of $Co_xZn_{1-x}Cr_{0.5}Fe_{0.5}O_4$ nanoparticles. *J. Inorg. Organomet. Polym.* **2015**, *25*, 747–754. [CrossRef]
15. Baykal, A.; Elmal, A.Z.; Sertkol, M.; Sözeri, H. Structural and Magnetic Properties of $NiCr_xFe_{2-x}O_4$ nanoparticles Synthesized via Microwave Method. *J. Supercond. Nov. Magn.* **2015**, *28*, 3405–3410. [CrossRef]

16. Güner, S.; Baykal, A.; Amir, M.; Güngüneş, H.; Geleri, M.; Sözeri, H.; Shirsath, S.E.; Sertkol, M. Synthesis and characterization of oleylamine capped $Mn_xFe_{1-x}Fe_2O_4$ nanocomposite: Magneto-optical properties, cation distribution and hyperfine interactions. *J. Alloys Compd.* **2016**, *888*, 675–686. [CrossRef]

17. Chen, R.; Wang, W.; Zhao, X.; Zhang, Y.; Wu, S.; Li, F. Rapid hydrothermal synthesis of magnetic $Co_xNi_{1-x}Fe_2O_4$ nanoparticles and their application on removal of Congo red. *Chem. Eng. J.* **2014**, *242*, 226–233. [CrossRef]

18. Maaz, K.; Khalid, W.; Mumtaz, A.; Hasanain, S.K.; Liu, J.; Duan, J.L. Magnetic characterization of $Co_{1-x}Ni_xFe_2O_4$ (0 < x < 1) nanoparticles prepared by co-precipitation route. *Phys. E Low-Dimens. Syst. Nanostruct.* **2009**, *41*, 593–599.

19. Salunkhe, A.B.; Khot, V.M.; Phadatare, M.R.; Thorat, N.D.; Joshi, R.S.; Yadav, H.M.; Pawar, S.H. Low temperature combustion synthesis and magnetostructural properties of Co–Mn nanoferrites. *J. Magn. Magn. Mater.* **2014**, *352*, 91–98. [CrossRef]

20. Almessiere, M.A.; Slimani, Y.; Ali, S.; Baykal, A.; Ercan, I.; Sozeri, H. Nd^{3+} Ion-Substituted $Co_{1-2x}Ni_xMn_xFe_{2-y}Nd_yO_4$ nanoparticles: Structural, Morphological, and Magnetic Investigations. *J. Inorg. Organomet. Polym. Mater.* **2018**, 1–91. [CrossRef]

21. Yadav, R.S.; Havlica, J.; Masilko, J.; Kalina, L.; Wasserbauer, J.; Hajdúchová, M.; Enev, V.; Kuřitka, I.; Kožáková, Z. Impact of Nd^{3+} in $CoFe_2O_4$ spinel ferrite nanoparticles on cation distribution, structural and magnetic properties. *J. Magn. Magn. Mater.* **2016**, *399*, 109–117. [CrossRef]

22. Tahar, L.B.; Artus, M.; Ammar, S.; Smiri, L.S.; Herbst, F.; Vaulay, M.J.; Richard, V.; Grenèche, J.M.; Villain, F.; Fiévet, F. Magnetic properties of $CoFe_{1.9}RE_{0.1}O_4$ nanoparticles (RE = La, Ce, Nd, Sm, Eu, Gd, Tb, Ho) prepared in polyol. *J. Magn. Magn. Mater.* **2008**, *320*, 3242–3250. [CrossRef]

23. Zhao, L.; Yang, H.; Zhao, X.; Yu, L.; Cui, Y.; Feng, S. Magnetic properties of $CoFe_2O_4$ ferrite doped with rare earth ion. *Mater. Lett.* **2006**, *60*, 1–6. [CrossRef]

24. Karaoglu, E.; Baykal, A.; Erdemi, H.; Alpsoy, L.; Sozeri, H. Synthesis and characterization of dl-thioctic acid (DLTA)–Fe_3O_4 nanocomposite. *J. Alloys Compd.* **2011**, *509*, 9218–9225. [CrossRef]

25. Garlyyev, B.; Durmus, Z.; Kemikli, N.; Sozeri, H.; Baykal, A.; Ozturk, R. Synthesis and magnetic properties of a porphine-based photosynthesizer with magnetic nano-carriers. *Polyhedron* **2011**, *30*, 2843–2848. [CrossRef]

26. Temizel, E.; Ayan, E.; Senel, M.; Erdemi, H.; Yavuz, M.S.; Kavas, H.; Baykal, A.; Öztürk, R. Synthesis, conductivity and magnetic properties of poly(N-pyrrole phosphonic acid)–Fe_3O_4 nanocomposite. *Mater. Chem. Phys.* **2011**, *131*, 284–291. [CrossRef]

27. Almessiere, M.A.; Slimani, Y.; Korkmaz, A.D.; Guner, S.; Sertkol, M.; Shirsath, S.E.; Baykal, A. Structural, optical and magnetic properties of Tm^{3+} substituted cobalt spinel ferrites synthesized via sonochemical approach. *Ultrason.–Sonochem.* **2019**. [CrossRef]

28. Almessiere, M.A. Magnetic and structural characterization of Nb^{3+}-substituted $CoFe_2O_4$ nanoparticles. *Ceram. Int.* **2019**. [CrossRef]

29. Li, X.; Hou, Y.; Zhao, Q.; Wang, L. A general, one-step and template-free synthesis of sphere-like zinc ferrite nanostructures with enhanced photocatalytic activity for dye degradation. *J. Colloid Interface Sci.* **2011**, *358*, 102. [CrossRef] [PubMed]

30. Stoner, E.C.; Wohlfarth, E.P. A Mechanism of Magnetic Hysteresis in Heterogeneous Alloys. *Philos. Trans. R. Soc. A* **1948**, *240*, 599–642. [CrossRef]

31. Almessiere, M.A.; Korkmaz, A.D.; Slimani, Y.; Nawaz, M.; Ali, S.; Baykal, A. Magneto-optical properties of rare earth metals substituted Co-Zn spinel nanoferrites. *Ceram. Int.* **2019**, *45*, 3449–3458. [CrossRef]

32. Almessiere, M.A.; Slimani, Y.; Baykal, A. Exchange spring magnetic behavior of $Sr_{0.3}Ba_{0.4}Pb_{0.3}Fe_{12}O_{19}/(CuFe_2O_4)_x$ nanocomposites fabricated by a one-pot citrate sol-gel combustion method. *J. Alloys Compd.* **2018**, *762*, 389–397. [CrossRef]

33. Duong, G.V.; Hanh, N.; Linh, D.V.; Groessinger, R.; Weinberger, P.; Schafler, E.; Zehetbauer, M. Monodispersed nanocrystalline $Co_{1-x}Zn_xFe_2O_4$ particles by forced hydrolysis: Synthesis and characterization. *J. Magn. Magn. Mater.* **2007**, *311*, 46–50. [CrossRef]

34. Slimani, Y.; Güngüneş, H.; Nawaz, M.; Manikandan, A.; el Sayed, H.S.; Almessiere, M.A.; Sözeri, H.; Shirsath, S.E.; Ercan, I.; Baykal, A. Magneto-optical and microstructural properties of spinel cubic copper ferrites with Li-Al co-substitution. *Ceram. Int.* **2018**, *44*, 14242–14250. [CrossRef]

35. Almessiere, M.A.; Slimani, Y.; Baykal, A. Structural and magnetic properties of Ce doped strontium hexaferrite. *Ceram. Int.* **2018**, *44*, 9000. [CrossRef]

36. Chen, F.X.; Jia, J.T.; Xu, Z.G.; Zhou, B.; Liao, C.S.; Yan, C.H.; Chen, L.Y.; Zhao, H.B. Microstructure, magnetic, and magneto-optical properties of chemical synthesized Co-RE (RE = Ho, Er, Tm, Yb, Lu) ferrite nanocrystalline films. *J. Appl. Phys.* **1999**, *86*, 2727. [CrossRef]

37. Kim, D.H.; Nikles, D.E.; Johnson, D.T.; Brazel, C.S. Heat generation of aqueously dispersed $CoFe_2O_4$ nanoparticles as heating agents for magnetically activated drug delivery and hyperthermia. *J. Magn. Magn. Mater.* **2008**, *320*, 2390–2396. [CrossRef]

38. Deraz, N.M. Effects of magnesia addition on structural, morphological and magnetic properties of nano-crystalline nickel ferrite system. *Ceram. Int.* **2012**, *38*, 511–516. [CrossRef]

39. Ahmad, M.R.; Jamil, Y.; Tabasuum, A.; Hussain, T. Refinement in the structural and magnetic properties of $Co_{0.5}Ni_{0.5}Fe_2O_4$ and its application as laser micro-propellant using ablation confinement. *J. Magn. Magn. Mater.* **2015**, *384*, 302–307. [CrossRef]

40. Sepelak, V.; Bergmann, I.; Feldhoff, A.; Heitjans, P.; Krumeich, F.; Menzel, D.; Litterst, F.J.; Campbell, S.J.; Becker, K.D. Nanocrystalline Nickel Ferrite, $NiFe_2O_4$: Mechanosynthesis, Nonequilibrium Cation Distribution, Canted Spin Arrangement, and Magnetic Behavior. *J. Phys. Chem. C* **2007**, *111*, 5026–5033. [CrossRef]

41. Slimani, Y.; Almessiere, M.A.; Nawaz, M.; Baykal, A.; Akhtar, S.; Ercan, I.; Belenli, I. Effect of bimetallic (Ca, Mg) substitution on magneto-optical properties of $NiFe_2O_4$ nanoparticles. *Ceram. Int.* **2018**. [CrossRef]

42. Coey, J.M.D. Noncollinear spin arrangement in ultrafine ferrimagnetic crystallites. *Phys. Rev. Lett.* **1971**, *27*, 1140–1142. [CrossRef]

43. Amir, M.; Gungunes, H.; Slimani, Y.; Tashkandi, N.; el Sayed, H.S.; Aldakheel, F.; Sertkol, M.; Sozeri, H.; Manikandan, A.; Ercan, I.; et al. Mossbauer studies and magnetic properties of cubic $CuFe_2O_4$ nanoparticles. *J. Supercond. Nov. Magn.* **2018**. [CrossRef]

44. Lin, Q.; He, Y.; Xu, J.; Lin, J.; Guo, Z.; Yang, F. Effects of Al^{3+} Substitution on Structural and Magnetic Behavior of $CoFe_2O_4$ Ferrite Nanomaterials. *Nanomaterials* **2018**, *8*, 750. [CrossRef] [PubMed]

45. Lin, J.; He, Y.; Du, X.; Lin, Q.; Yang, H.; Shen, H. Structural and Magnetic Studies of Cr^{3+} Substituted Nickel Ferrite Nanomaterials Prepared by Sol-Gel Auto-Combustion. *Crystals* **2018**, *8*, 384. [CrossRef]

46. Ali, I.; Islam, M.U.; Awan, M.S.; Ahmad, M.; Ashiq, M.N.; Naseem, S. Effect of Tb^{3+} substitution on the structural and magnetic properties of M-type hexaferrites synthesized by sol–gel auto-combustion technique. *J. Alloy. Compd.* **2013**, *550*, 564–572. [CrossRef]